Inorg. Chem. **2005**, *44*, 3605–3617

Inorganic Chemistry Article

Spectroscopic and Computational Studies on [Ni(tmc)CH_3]OTf: Implications for Ni–Methyl Bonding in the A Cluster of Acetyl-CoA Synthase

Ralph Schenker,[†] Michael T. Mock,[‡] Matthew T. Kieber-Emmons,[‡] Charles G. Riordan,[‡] and Thomas C. Brunold[*,†]

Department of Chemistry, University of Wisconsin—Madison, Madison, Wisconsin 53706, and Department of Chemistry and Biochemistry, University of Delaware, Newark, Delaware 19716

Received November 14, 2004

The five-coordinate high-spin ($S = 1$) Ni^{2+} complex $[Ni(tmc)CH_3]^+$ (**1**) (tmc = 1,4,8,11-tetramethyl-1,4,8,11-tetraazacyclotetradecane) serves as a model for a viable reaction intermediate of the A cluster of acetyl-CoA synthase (ACS) in which the distal nickel center is methylated. Spectroscopic and density functional theory (DFT) computational studies afford a quantitative bonding description for **1** that reveals a highly covalent Ni–CH_3 bond. From a normal coordinate analysis of resonance Raman data obtained for **1**, a value of $k_{Ni-C} = 1.44$ mdyn/Å is obtained for the Ni–C stretch force constant of this species. This value is smaller than $k_{Co-C} = 1.85$ mdyn/Å, which is reported for the Co–C stretch in the methylcobinamide cofactor (**5**) that serves as the methyl donor to the A cluster in the ACS catalytic cycle. Experimentally calibrated DFT computations on viable methylated A cluster models reveal that the methyl group binds to the proximal (Ni_p) rather than the distal (Ni_d) nickel center and afford a simple electronic argument for this preference. By correlating the experimental force constants with the computed bond orders of the M–C bonds in **1** and **5**, the Ni_p^{2+}–CH_3 bond strength for an A cluster model with a square-planar Ni_p conformation, which is the most probable structure of the methylated A cluster on the basis of steric and energetic considerations, is predicted to be similar to the Co^{3+}–CH_3 bond strength in CH_3–CoFeSP. This similarity could be a crucial thermodynamic prerequisite for the reversibility of the enzymatic transmethylation reaction.

Introduction

Acetyl-CoA synthase (ACS) is employed by acetogenic, methanogenic, and sulfate-reducing archaea and bacteria as part of the Wood–Ljungdahl pathway to grow autotropically on H_2 and CO_2.[1,2] In the acetogen *Moorella thermoacetica*, ACS is paired with CO dehydrogenase (CODH) to form a bifunctional enzyme (ACS/$CODH_{Mt}$), whereas in the hydrogenogen *Carboxythermus hydrogenoformans*, it exists both as a bifunctional ACS/$CODH_{Ch}$ and a monofunctional ACS_{Ch}.[3] The reaction catalyzed by ACS (eq 1), conducted at the so-called A cluster, comprises the reversible formation of acetyl-CoA from coenzyme A, CO, and a methyl group provided by a methylated corrinoid iron–sulfur protein (CH_3–Co^{3+}FeSP):[2,4]

$$CO + CoA^- + CH_3{-}Co^{3+}FeSP \leftrightarrow acetyl\text{-}CoA + Co^{+}FeSP \quad (1)$$

Recent X-ray crystallographic studies revealed that the A cluster consists of a $[Fe_4S_4]$ unit linked via a cysteine bridge to a proximal metal that, in turn, is connected to a square-planar, distal Ni site via two cysteine bridges (Figure 1).[3,5,6] The identity of the catalytically relevant metal ion in the proximal site has been the subject of some debate. Whereas in one structure this site contains either Cu or Zn in distorted

---

[*] Author to whom correspondence should be addressed. E-mail: brunold@chem.wisc.edu.

[†] University of Wisconsin—Madison.

[‡] University of Delaware.

(1) (a) Ferry, J. G. *Crit. Rev. Biochem. Mol. Biol.* **1992**, *27*, 473–503. (b) Lindahl, P. A. *Biochemistry* **2002**, *41*, 2097–2105.

(2) Ragsdale, S. W.; Kumar, M. *Chem. Rev.* **1996**, *96*, 2515–2539.

(3) Svetlitchnyi, V.; Dobbek, H.; Meyer-Klaucke, W.; Meins, T.; Thiele, B.; Römer, P.; Huber, R.; Meyer, O. *Proc. Natl. Acad. Sci. U.S.A.* **2004**, *101*, 446–451.

(4) Ragsdale, S. W.; Wood, H. G. *J. Biol. Chem.* **1985**, *260*, 3970–3977.

(5) Doukov, T. I.; Iverson, T. M.; Seravalli, J.; Ragsdale, S. W.; Drennan, C. L. *Science* **2002**, *298*, 567–572.

(6) Darnault, C.; Volbeda, A.; Kim, E. J.; Legrand, P.; Vernède, X.; Lindahl, P. A.; Fontecilla-Camps, J. C. *Nat. Struct. Biol.* **2003**, *10*, 271–279.

10.1021/ic0483996 CCC: $30.25

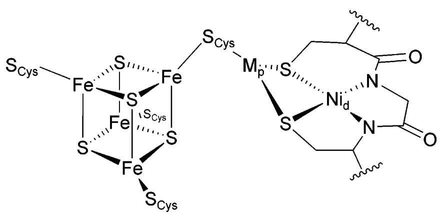

Figure 1. Schematic representation of the ACS A cluster. The proximal metal site M_p can be occupied by Ni, Cu, or Zn.[3,5,6] Exogenous ligands coordinated to M_p are omitted.

tetrahedral ligand environments,[5,6] in the other it is occupied by Ni ions adopting either approximate square-planar or tetrahedral coordination geometries.[3,6] Subsequent enzymatic,[7,8] spectroscopic,[9] and computational[10,11] studies provided compelling evidence that the catalytically active form contains Ni at the proximal site, whereas Cu functions as a potent inhibitor in vitro.[7,8] The structure of the A cluster with two configurationally distinct Ni sites and the intrinsic metal heterogeneity of the proximal site provide a logical explanation for the earlier observation[12] that the A cluster possesses a labile Ni center subject to removal by 1,10-phenanthroline (phen) as well as a nonlabile Ni site. These centers can now be identified as the proximal and distal Ni sites, respectively.[8]

Among the key steps in ACS catalysis is the methyl transfer from $CH_3{-}Co^{3+}$FeSP to the ACS A cluster. The methyl group is transferred as a CH_3^+ cation equivalent in an S_N2-type reaction according to eq 2.[13] A particularly remarkable aspect of this reaction is the formation of an extremely nucleophilic Co^+ center.[14]

$$\mathrm{ACS}^{n+} + \mathrm{CH_3{-}Co^{3+}FeSP} \Leftrightarrow \mathrm{CH_3{-}ACS}^{(n+2)+} + \mathrm{Co^{+}FeSP} \qquad (2)$$

Methylation of the A cluster requires the presence of a reducing agent such as dithionite.[15] Although the identity of the site in the A cluster undergoing reduction and the metal ion oxidation states are still the subject of intense debate,[5−7] the products of the reaction have been established. In the absence of CO, methylation yields a stable, EPR silent (i.e., $S = 0$ or 1) A cluster state that can subsequently be reacted with CO and CoA^- to yield acetyl-CoA.[15] An important step toward the development of a detailed understanding of how nature ensures the reversibility of the transmethylation reaction between the A cluster and $CH_3{-}Co^{3+}$FeSP (eq 2) involves exploring the geometric and electronic properties of the methylated A cluster intermediate. Although the identity of the Ni center to which the methyl group binds has not yet been directly established, Barondeau and Lindahl have shown that the A cluster lacking the labile Ni center cannot be methylated and methylation of the A cluster inhibits the removal of the labile Ni ion by phen, presumably by blocking one of the cis coordination sites.[15] Although these observations, along with recent computational evidence,[11] appear to indicate that the methyl group binds to the labile (i.e., proximal) Ni center, it has also been proposed that the methyl transfer instead involves the distal Ni center.[5,16,17]

Detailed spectroscopic and computational studies on synthetic complexes offer an opportunity to probe $Ni{-}CH_3$ bonding in a well-defined model system. Holm and coworkers have reported several $Ni{-}CH_3$ species possessing partial sulfur ligation that are part of the reaction sequence $[Ni] \rightarrow [Ni{-}CH_3] \rightarrow [Ni{-}C(O)CH_3] \rightarrow [Ni] +$ thioester, which mimics key steps in the proposed ACS catalytic cycle. The trigonal-bipyramidal complex $[Ni^{2+}\{N(C_2H_4{-}SR)_3\}{-}CH_3]^{2+}$ ($R = {}^{i}Pr, {}^{t}Bu$) binds CO to yield the acetyl derivative $[Ni^{2+}\{C(O)CH_3\}{-}\{N(C_2H_4SR)_3\}]^+$ that slowly reacts with thiols to form the corresponding thioester, Ni^0, and the protonated free ligand $HN(C_2H_4SR)_3{}^+$.[18] Tucci and Holm described the reaction of the square-planar species $[Ni^{2+}(bpy)(SR)CH_3]$ with 1 equiv of CO to afford a stable acetyl−thiolato nickel complex that further reacts with CO to yield $RSC(O)CH_3$ and $[Ni^0(bpy)(CO)_2]$ (bpy = 2,2′-bipyridine).[19] A particularly productive synthetic route for the preparation of a methylated A cluster model was pursued by one of us, involving the generation of the $Ni^{2+}{-}CH_3$ species $[Ni^{2+}(tmc)CH_3]^+$ (**1**) (tmc = 1,4,8,11-tetramethyl-1,4,8,11-tetraazacyclotetradecane) by transferring the methyl group from a $Co^{3+}{-}CH_3$ complex to the Ni^+ precursor $[Ni(tmc)]^+$, thereby mimicking a key step of the ACS catalytic cycle (note that a radical mechanism was shown to be operative in the synthetic system, involving a 1:2 stoichiometry in which one $[Ni(tmc)]^+$ complex reduces the $Co^{3+}{-}CH_3$ complex to generate a methyl radical that then reacts with a second molecule of $[Ni(tmc)]^+$).[20] This crystallographically characterized complex possesses a five-coordinate $S = 1$ Ni^{2+} center with the methyl group in the apical position, thus making it especially suitable for evaluating the likelihood of a $Ni_d{-}CH_3$ reaction intermediate.

In this study, absorption, magnetic circular dichroism (MCD), and variable-temperature variable-field MCD (VTVH-MCD) spectroscopic techniques have been employed in conjunction with density functional theory (DFT) electronic

---

(7) Bramlett, M. R.; Tan, X.; Lindahl, P. A. *J. Am. Chem. Soc.* **2003**, *125*, 9316−9317.

(8) Seravalli, J.; Xiao, Y.; Gu, W.; Cramer, S. P.; Antholine, W. E.; Krymov, V.; Gerfen, G. J.; Ragsdale, S. W. *Biochemistry* **2004**, *43*, 3944−3955.

(9) Chen, J.; Huang, S.; Seravalli, J.; Gutzman, H., Jr.; Swartz, D. J.; Ragsdale, S. W.; Bagley, K. A. *Biochemistry* **2003**, *42*, 14822−14830.

(10) Schenker, R. P.; Brunold, T. C. *J. Am. Chem. Soc.* **2003**, *125*, 13962−13963.

(11) Webster, C. E.; Darensbourg, M. Y.; Lindahl, P. A.; Hall, M. B. *J. Am. Chem. Soc.* **2004**, *126*, 3410−3411.

(12) Russel, W. K.; Stålhandske, C. M. V.; Xia, J.; Scott, R. A.; Lindahl, P. A. *J. Am. Chem. Soc.* **1998**, *120*, 7502−7510.

(13) Menon, S.; Ragsdale, S. W. *J. Biol. Chem.* **1999**, *274*, 11513−11518.

(14) Kumar, M.; Qui, D.; Spiro, T. G.; Ragsdale, S. W. *Science* **1995**, *270*, 628−630.

(15) Barondeau, D. P.; Lindahl, P. A. *J. Am. Chem. Soc.* **1997**, *119*, 3959−3970.

(16) Seravalli, J.; Gu, W.; Tam, A.; Strauss, E.; Begley, T. P.; Cramer, S. P.; Ragsdale, S. W. *Proc. Natl. Acad. Sci. U.S.A.* **2003**, *100*, 3689−3694.

(17) Grahame, D. A. *Trends Biochem. Sci.* **2003**, *28*, 221−224.

(18) (a) Stavropoulos, P.; Carrié, M.; Muetterties, M. C.; Holm, R. H. *J. Am. Chem. Soc.* **1990**, *112*, 5385−5387. (b) Stavropoulos, P.; Carrié, M.; Muetterties, M. C.; Holm, R. H. *J. Am. Chem. Soc.* **1991**, *113*, 8485−8492.

(19) Tucci, G. C.; Holm, R. H. *J. Am. Chem. Soc.* **1995**, *117*, 6489−6496.

(20) Ram, M. S.; Riordan, C. G.; Yap, G. P. A.; Liable-Sands, L.; Rheingold, A. L.; Marchaj, A.; Norton, J. R. *J. Am. Chem. Soc.* **1997**, *119*, 1648−1655.

structure calculations to generate an experimentally validated description of Ni−C bonding in **1**. The corresponding Ni−C bond strength has been determined from a normal coordinate analysis (NCA) of our resonance Raman (rR) spectroscopic data. Additionally, DFT computations on the methylated corrinoid cofactor in $\mathrm{CH_3{-}Co^{3+}}$FeSP and hypothetical models of the methylated A cluster have been performed to allow for a comparison of Ni−C and Co−C bonding in an effort to assess the likelihood of methyl binding to the proximal and distal Ni centers.

Experimental Methods

Sample Preparation. Samples of $[\mathrm{Ni(tmc)CH_3}]$OTf (**1**) ($\mathrm{OTf^-} = \mathrm{CF_3SO_3^-}$)[21] were obtained upon reaction of the $\mathrm{Ni^{2+}}$ precursor (*R*,*R*,*S*,*S*)-$[\mathrm{Ni(tmc)}](\mathrm{OTf})_2$ with $(\mathrm{CH_3})_2\mathrm{Mg}$. All preparations were performed in a drybox under an argon atmosphere. In a typical reaction, 150 mg of the pink complex (*R*,*R*,*S*,*S*)-$[\mathrm{Ni(tmc)}](\mathrm{OTf})_2$ were suspended in 30 mL of tetrahydrofuran (THF). A solution of $(\mathrm{CH_3})_2\mathrm{Mg}$ (0.03 M) in THF was added dropwise to the stirring heterogeneous mixture, resulting in a bright green solution. The addition was continued until almost all of the pink starting material was consumed. Overshooting this end point resulted in a gray-brown solution and lower isolated yields. The bright green solution was filtered through a Celite plug to remove Mg salts and unreacted starting material. The filtrate was concentrated, and pentane was added to precipitate a bright green solid, which was collected, washed with $\mathrm{Et_2O}$, and dried in vacuo (yield: ∼80%). This product was characterized by NMR and UV−vis spectroscopy.[19] For MCD spectroscopy, the sample was ground in a mortar. Poly(dimethylsiloxane) was added to the light green powder and thoroughly mixed to obtain a mull, which was then suspended between the two quartz glass disks of an MCD sample cell. For rR spectroscopy, sample material was mixed with $\mathrm{K_2SO_4}$ in a ∼1:1 ratio and thoroughly ground in a mortar. The resulting fine powder was transferred into an NMR tube that was sealed with a plastic cap and Parafilm. After removal from the drybox, all samples were immediately frozen in liquid $\mathrm{N_2}$.

Spectroscopy. Absorption and MCD spectra of a solid-state mull of **1** in poly(dimethylsiloxane) were recorded at various temperatures between 4 and 50 K using a spectropolarimeter (Jasco J-715) with a sample compartment modified to accommodate a superconducting magnetocryostat (Oxford Instruments SM-4000). VTVH-MCD data were fit using the software developed by Dr. Frank Neese (MPI Mülheim, Germany). rR spectra of isotopically pure samples of **1** prepared with either $(\mathrm{CH_3})_2\mathrm{Mg}$ or $(\mathrm{CD_3})_2\mathrm{Mg}$ were recorded upon excitation with $\mathrm{Ar^+}$ (Coherent I-305) or $\mathrm{Kr^+}$ (Coherent I-302) ion lasers with an incident laser power of 10−15 mW at the sample, which was contained in an NMR tube at 77 K using a liquid-$\mathrm{N_2}$-filled EPR Dewar. The scattered light was collected at a backscattering angle of ∼135°, dispersed by a triple monochromator (Acton Research) using 1200 and 2400 grooves/mm gratings, and detected by a back-illuminated CCD camera (Princeton Instruments, 1340 × 100 pixels). Raman shifts and intensities were calibrated relative to the 984 $\mathrm{cm^{-1}}$ peak of $\mathrm{K_2SO_4}$, which was added to the samples as an internal standard.

NCA. A NCA of the vibrational data of **1** was performed on the $\mathrm{NiN_4C}$ core assuming an idealized C_{4v} geometry with Ni−C and Ni−N bond lengths of 2.065 and 2.196 Å, respectively, and a C−Ni−N bond angle of 100.0°, as derived from the DFT geometry-optimized model of **1** (vide infra). The analysis was based on the Wilson FG matrix method using a Urey−Bradley force field as implemented in a modified version of the Schachtschneider program.[22]

Chart 1. Positions of the C Atoms Represented by ● Were Kept Frozen during DFT Geometry Optimization

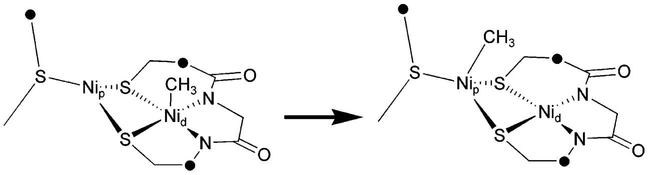

2a (*S* = 1)
2b (*S* = 0)

3a (*S* = 1)
3b (*S* = 0)

Chart 2. Positions of the C Atoms Represented by ● Were Kept Frozen during DFT Geometry Optimization

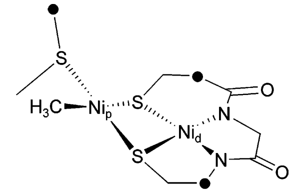

4

Electronic Structure Calculations. DFT computations were performed on a cluster composed of 20 Intel Xeon 2.4 GHz processors (Ace Computers) using the Amsterdam Density Functional (ADF) 2003.01 software package.[23] The computational model comprised the complete molecular structure of **1**, using the atomic coordinates of the crystallographically characterized compound (*R*,*R*,*S*,*S*)-$[\mathrm{Ni(tmc)CH_3}](\mathrm{BAr'_4})$[20] as starting values. Initial atomic positions for the A cluster models **2**−**4** (Charts 1 and 2) were taken from the $[\mathrm{Fe_4S_4}]^{2+}{-}\mathrm{Ni_p}^{+}\mathrm{CO}{-}\mathrm{Ni_d}^{2+}$ model employed in our previous calculations[10] but using a methyl group instead of the $[\mathrm{Fe_4S_4}]$ unit. This truncation scheme was chosen over other viable schemes for two primary reasons: (i) Modeling the diamagnetic $[\mathrm{Fe_4S_4}]^{2+}$ cluster by a mononuclear high spin ($S = 2$) $\mathrm{Fe^{2+}}$ center, as in ref 11, may drastically alter the electronic properties of the $\mathrm{Ni_p}$ center as a result of exchange interactions between the two metals, and (ii) a similar approach was used successfully in previous computations on the active-site cluster of Fe-only hydrogenases (the so-called H cluster).[24] Atomic coordinates for $\mathrm{MeCbi^+}$ (model **5**, Chart 3), which weakly binds a water molecule in the lower axial position, were taken from ref 25. For all models, refined atomic coordinates were obtained through DFT energy minimizations using the algorithm of Versluis and Ziegler.[26] For the A cluster models **2**−**4**, the positions of the C atoms, represented by ● in Charts 1 and 2,

---

(21) Abbreviations: tmc, tetramethylcyclam; $\mathrm{OTf^-}$, triflate, $\mathrm{CF_3SO_3^-}$; $(\mathrm{BAr'_4})$, $\mathrm{B\{3,\,5\text{-}(CF_3)_2(C_6H_3)_4\}^-}$.

(22) (a) Schachtschneider, J. H. Technical Report No. 57-65; Shell Development Company: Emeryville, CA, 1966. (b) Fuhrer, H.; Kartha, V. B.; Kidd, K. G.; Krueger, P. J.; Mantsch, H. H. *Computer Programs for Infrared Spectroscopy*; Bulletin No. 15; National Research Council of Canada: Ottawa, 1976.

(23) (a) Baerends, E. J.; Ellis, D. E.; Ros, P. *Chem. Phys.* **1973**, *2*, 41−51. (b) te Velde, G.; Baerends, E. J. *Int. J. Comput. Phys.* **1992**, *99*, 84−98.

(24) (a) Fan, H.-J.; Hall, M. B. *J. Am. Chem. Soc.* **2001**, *123*, 3828−3829. (b) Bruschi, M.; Fantucci, P.; De Gioia, L. *Inorg. Chem.* **2002**, *41*, 1421−1429. (c) Liu, Z.-P.; Hu, P. *J. Am. Chem. Soc.* **2002**, *124*, 5175−5182. (d) Georgakaki, I. P.; Thomson, L. M.; Lyon, E. J.; Hall, M. B.; Darensbourg, M. Y. *Coord. Chem. Rev.* **2003**, *238−239*, 255−266.

(25) Stich, T. A.; Brooks, A. J.; Buan, N. R.; Brunold, T. C. *J. Am. Chem. Soc.* **2003**, *125*, 5897−5914.

(26) Versluis, L.; Ziegler, T. *J. Chem. Phys.* **1988**, *88*, 322−329.

Chart 3

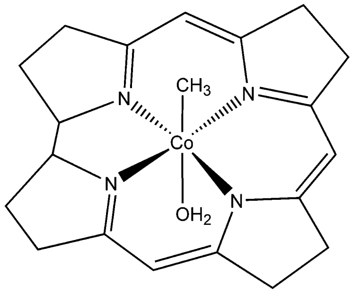

5

were kept frozen to account for the constraints imposed by the protein backbone. All computations were carried out using an integration constant of 4.0, the Vosko−Wilk−Nusair local density approximation[27] (LDA) for the exchange and correlation energies, and the nonlocal gradient corrections of Becke[28] and Perdew.[29] A triple-ζ Slater-type orbital (STO) basis set with a single-ζ STO polarization function (ADF basis set IV) was used for all of the atoms. Core orbitals were frozen through 1s (C, N) and 2p (Ni). The atomic coordinates for all of the models described in the text are included in the Supporting Information (Tables S1−S8).

Because of the large number of different density functionals implemented in the ORCA 2.2.73 software package developed by Dr. Frank Neese, this program was used for single point calculations on the optimized models **1**−**5**.[30] Pure DFT computations were carried out using a Perdew−Wang parametrization of the LDA (PW-LDA)[31] with the nonlocal gradient corrections of Becke[28] and Perdew[29] (BP). Alternatively, hybrid DFT calculations were performed employing Becke's three-parameter hybrid functional[32] for exchange together with the Lee−Yang−Parr correlation functional (B3LYP/G),[33] whereby the Hartree−Fock exchange contribution was varied between 5 and 25%. In all computations, a triple-ζ Gaussian-type orbital (Ahlrich's TZV)[34] basis set was chosen with three, two, and one polarization functions for the Ni, methyl-C, and N atoms, respectively.[35] The remaining atoms were modeled with the SV(P) (Ahlrich's polarized split valence) basis set.[34] The SV/J[36] and SV/C[37] auxiliary basis sets were used for calculations with pure DFT and hybrid functionals, respectively, and an integration grid of size 4 (Lebedev 302 points) was employed in each case.

Vertical excitation energies and transition dipole moments were calculated by the time-dependent DFT (TD-DFT) method[38] within the Tamm−Dancoff approximation,[39] as implemented in ORCA, employing the same functionals and basis sets as described above for the ground-state calculations. Convergence of the TD-DFT calculations required the use of the resolution of the identity approximation in calculating the Coulomb term.[40] Ninety excited states were calculated by including all one-electron excitations within an energy window of ±3 Hartrees with respect to the HOMO/LUMO energies. Isosurface plots of MOs, electron density difference maps (EDDMs), and the total unpaired spin density distribution obtained from the spin-unrestricted ORCA calculations were generated with the gOpenMol software program developed by Leif Laaksonen (using isodensity values of 0.05, 0.005, and 0.01 a.u., respectively).[41]

The ORCA software was also used to calculate transition energies and dipole moments as well as the ground-state spin Hamiltonian parameters for the DFT geometry-optimized model of **1** within the framework of semiempirical INDO/S-CI calculations. ORCA utilizes the INDO/S model of Zerner and co-workers,[42] the valence shell ionization potentials and Slater−Condon parameters listed by Bacon and Zerner,[43] and the standard interaction factors $f_{p\sigma p\sigma} = 1.266$ and $f_{p\pi p\pi} = 0.585$. A restricted open-shell Hartree−Fock self-consistent field calculation was tightly converged on the spin-triplet ground state, which served as the reference state for configuration interaction (CI) calculations. For the calculation of the ground state properties, the largest achievable active space included all possible single excitations within 76 MOs [including all 61 doubly occupied MOs (DOMOs), the 2 singly occupied MOs (SOMOs), and the lowest 13 virtual MOs] as well as double excitations within 70 MOs (including all 61 DOMOs, the SOMOs, and the lowest 7 virtual MOs). To calculate transition energies and oscillator strengths, all possible spin-allowed single excitations into the SOMOs and virtual MOs plus the spin-forbidden excitations involving the two SOMOs were considered.

Results and Analysis

A. Spectroscopy. A.1. Absorption and rR. The 4 K solid-state mull absorption spectrum of **1** is dominated by an intense broad feature centered at 40 500 cm^{-1} that is accompanied by a less-intense band peaking at 28 500 cm^{-1} with a weak shoulder at 24 000 cm^{-1} (Figure 2). Additional, weak bands can be discerned at 15 000 and 20 000 cm^{-1}. To identify the nature of the corresponding transitions, rR data were collected using various excitation wavelengths. The rR spectrum for the 407 nm (24 588 cm^{-1}) excitation of **1** prepared with $(CH_3)_2Mg$ (**1-CH$_3$**) is dominated by two intense peaks at 117 and 232 cm^{-1} (Figure 3). Although the former peak downshifts slightly to 115 cm^{-1} for samples

---

(27) Vosko, S. H.; Wilk, L.; Nusair, M. *Can. J. Phys.* **1980**, *58*, 1200−1211.

(28) Becke, A. D. *J. Chem. Phys.* **1986**, *84*, 4524−4529.

(29) Perdew, J. P. *Phys. Rev. B: Condens. Matter* **1986**, *33*, 8822−8824.

(30) Neese, F., Max Planck Institute for Bioinorganic Chemistry, D-45470 Mülheim/Ruhr, Germany. E-mail: neese@mpi-muelheim.mpg.de.

(31) Perdew, J. P.; Wang, Y. *Phys. Rev. B: Condens. Matter* **1992**, *45*, 13244−13249.

(32) (a) Becke, A. D. *J. Chem. Phys.* **1993**, *98*, 1372−1377. (b) Becke, A. D. *J. Chem. Phys.* **1993**, *98*, 5648−5652.

(33) Lee, C.; Yang, W.; Parr, R. G. *Phys. Rev. B: Condens. Matter* **1988**, *37*, 785−789.

(34) Schäfer, A.; Horn, H.; Ahlrichs, R. *J. Chem. Phys.* **1992**, *97*, 2571−2577.

(35) The Ahlrichs (2d, 2p, 2d2fg, and 3p2df) polarization functions were obtained from the TurboMole basis set library at ftp://ftp.chemie.uni-karlsruhe.de/pub/cbasen.

(36) The Ahlrichs auxiliary basis sets were obtained from the TurboMole basis set library at ftp://ftp.chemie.uni-karlsruhe.de/pub/cbasen. (a) Eichkorn, K.; Treutler, O.; Ohm, H.; Haser, M.; Ahlrichs, R. *Chem. Phys. Lett.* **1995**, *240*, 283−290. (b) Eichkorn, K.; Weigend, F.; Treutler, O.; Ahlrichs, R. *Theor. Chem. Acc.* **1997**, *97*, 119−124.

(37) The Ahlrichs auxiliary basis sets were obtained from the TurboMole basis set library at ftp://ftp.chemie.uni-karlsruhe.de/pub/cbasen. Weigend, F.; Häser, M. *Theor. Chem. Acc.* **1997**, *97*, 331−340.

(38) (a) Bauernschmitt, R.; Ahlrichs, R. *Chem. Phys. Lett.* **1996**, *256*, 454−464. (b) Casida, E. M.; Jamorski, C.; Casida, K. C.; Salahub, D. R. *J. Chem. Phys.* **1998**, *108*, 4439−4449. (c) Stratman, R. E.; Scuseria, G. E.; Frisch, M. J. *J. Chem. Phys.* **1998**, *109*, 8218−8224.

(39) (a) Hirata, S.; Head-Gordon, M. *Chem. Phys. Lett.* **1999**, *302*, 375−382. (b) Hirata, S.; Head-Gordon, M. *Chem. Phys. Lett.* **1999**, *314*, 291−299.

(40) Neese, F.; Olbrich, G. *Chem. Phys. Lett.* **2002**, *362*, 170−178.

(41) (a) Laaksonen, L. *J. Mol. Graphics* **1992**, *10*, 33−34. (b) Bergman, D. L.; Laaksonen, L.; Laaksonen, A. *J. Mol. Graphics Modell.* **1997**, *15*, 301−306.

(42) (a) Ridley, J.; Zerner, M. C. *Theor. Chim. Acta* **1973**, *32*, 111. (b) Zerner, M. C.; Loew, G. H.; Kirchner, R. F.; Mueller-Westerhof, U. T. *J. Am. Chem. Soc.* **1980**, *102*, 589−599.

(43) Bacon, A. D.; Zerner, M. C. *Theor. Chim. Acta* **1979**, *53*, 21−54.

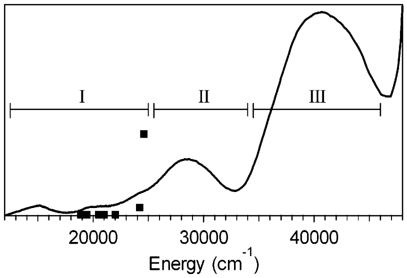

Figure 2. A 4 K solid-state mull absorption spectrum (solid line) of **1** superimposed by the rR excitation profile (■) of the collective intensities of the dominant vibrational features observed at 117 and 232 cm^{-1}. The spectrum is divided into three regions labeled I, II, and III that are associated with LF, C → Ni CT, and N → Ni CT transitions, respectively.

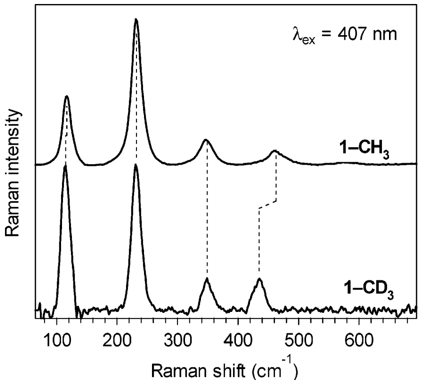

Figure 3. A 77 K rR spectra for the 407 nm (24 588 cm^{-1}) excitation of **1** prepared with $(CH_3)_2Mg$ (**1-CH$_3$**, top) and $(CD_3)_2Mg$ (**1-CD$_3$**, bottom).

prepared with $(CD_3)_2Mg$ (**1-CD$_3$**), the latter is insensitive to this isotopic substitution. Two additional, weak features at 348 and 463 cm^{-1} are observed in the spectrum of **1-CH$_3$**, of which only the latter is isotope-sensitive, downshifting to 435 cm^{-1} in **1-CD$_3$**. This isotopic shift of 28 cm^{-1} compares fairly well with the value of 32 cm^{-1} calculated for a simple Ni−methyl harmonic oscillator, permitting the assignment of the 463/435 cm^{-1} feature as the Ni−C stretching mode. The frequency of the 117/115 cm^{-1} feature is too low for it to correspond to a stretching mode; instead, we assign this feature to a C−Ni−N bend. The isotope-insensitive 232 and 348 cm^{-1} bands cannot be readily assigned. Their identities will be explored in Section C.1.

The rR excitation profile of the collective intensities of the 117 and 232 cm^{-1} features of **1-CH$_3$** traces the onset of the 28 500 cm^{-1} absorption band [Figure 2; note that laser excitation at wavelengths below 407 nm (>24 588 cm^{-1}) led to photodecomposition of the sample].[44] Because of the low intensity of the 463 cm^{-1} rR feature, its excitation profile could not be determined accurately; however, it appears to mirror that of the two dominant rR bands shown in Figure 2. The fact that the Ni−C stretch is enhanced upon excitation into the 28 500 cm^{-1} absorption band indicates that the corresponding transition contains substantial C → Ni charge-transfer (CT) character.

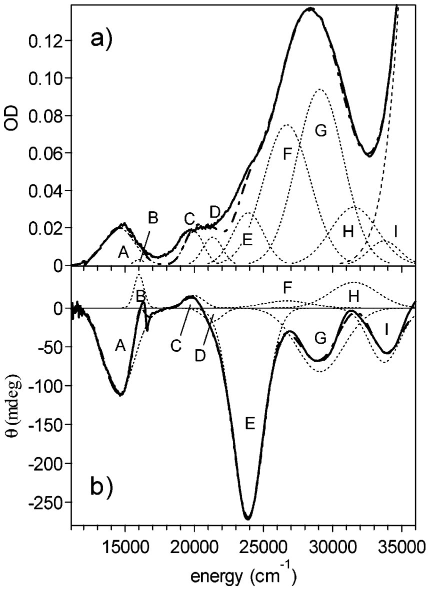

Figure 4. Solid-state mull absorption (a) and 7 T MCD spectra (b) of **1** at 4 K (solid lines). The dotted lines represent Gaussian band shape simulations for transitions A−I obtained using the fit parameters in Table 1. Their sums are shown by the dashed lines. The thin dashed line in the absorption spectrum serves to model the onset to the 40 500 cm^{-1} band (Figure 2).

Table 1. Fit Parameters from an Iterative Gaussian Deconvolution of the Absorption and MCD Spectra of **1** in Figure 4[a]

band	ν_{max}	fwhm	OD	q	$\lvert\theta\rvert$/OD	assign.[b]
A	14 560	2625	0.020	−110	5500	LF
B	16 000	830	0.003	+43	14333	LF
C	19 980	1665	0.018	+16	888	LF
D	21 325	1665	0.015	−17	1133	LF
E	23 900	2625	0.028	−271	9678	CT
F	26 700	4000	0.075	+9	120	CT
G	29 100	4000	0.094	−82	872	CT
H	31 550	4000	0.031	+33	1065	CT
I	33 740	2625	0.013	−70	5385	CT

[a] Band positions (ν_{max}) and bandwidth at half-maximum (fwhm) are given in cm^{-1}. The absorption intensity and magnetic ellipticity (θ) are given in units of optical density (OD) and mdeg, respectively. [b] Band assignments (see text for details).[46]

A.2. MCD and VTVH-MCD. To aid in the resolution of overlapping absorption bands and to determine the spin Hamiltonian parameters characterizing the $S = 1$ ground state of **1**, MCD spectra were measured at various fixed temperatures between 4 and 50 K. The MCD intensity was found to be strongly temperature-dependent, consistent with the expected MCD C-term behavior for this paramagnetic species (vide infra). The 4 K MCD spectrum shown in Figure 4b exhibits several intense, predominantly negatively signed features. To determine the number and intensities of the transitions contributing to the spectrum in the 12 000−35 000 cm^{-1} range, iterative fits of the absorption and MCD spectra were performed using Gaussians with fixed bandwidths. In this fitting procedure, the lowest number of bands was sought that yielded reasonable agreement between the simulated and experimental spectra. Acceptable fits required a minimum of nine Gaussian bands (i.e., although fits with fewer bands failed to reproduce all of the features in the experimental absorption and MCD spectra, the inclusion of additional bands did not notably improve the quality of the fits), corresponding to transitions A−I in Figure 4 and Table 1. This Gaussian deconvolution reveals that the absorption

---

[44] This conclusion is supported by the observation of a color change of the sample from light green to brown at the spot irradiated by the laser beam.

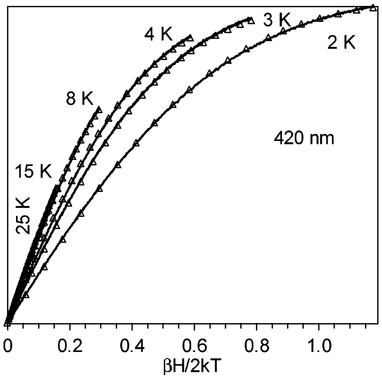

Figure 5. Experimental VTVH-MCD data at 420 nm (21 810 cm^{-1}, band E) for **1** (solid lines). Simulated data (△) were obtained with the parameters $D = -8.75$ cm^{-1}, $E/D = 0.25$, and $g = 2.20$ and the fitted molecular polarizations $\%x = 0.5$, $\%y = 4.5$, and $\%z = 95.0$.

feature at 28 500 cm^{-1} actually consists of three components (transitions F−H) that are relatively weak in the MCD spectrum but intense in absorption. This behavior is characteristic of CT transitions, which typically give rise to small $|\theta|$/OD ratios (where θ and OD denote the MCD ellipticity[45] and the absorption optical density, respectively, used here instead of $\Delta\epsilon$ and ϵ values because the latter cannot be obtained from mull spectra).[46] In comparison, the $|\theta|$/OD ratios for bands A−E and I are roughly 1 order of magnitude larger, allowing for their assignment as ligand-field (LF) transitions. Band B at 16 000 cm^{-1} is particularly sharp and has virtually no absorption intensity, indicating that it corresponds to a spin-forbidden intraconfigurational (spin-flip) transition. Bands C and D at 19 980 and 21 325 cm^{-1}, respectively, have almost equal intensities but opposite signs in the MCD spectrum. This behavior is characteristic of a pseudo-A term involving two perpendicularly polarized transitions.[47]

Information regarding the molecular polarization of a given transition can be obtained from an analysis of the field and temperature dependencies of the corresponding MCD signal intensity. Such VTVH-MCD data were collected at 700 nm (14 286 cm^{-1}, band A) and 420 nm (21 810 cm^{-1}, band E) by sweeping the magnetic field between 0 and 7 T at numerous fixed temperatures between 2 and 50 K.[48] Figure 5 shows normalized VTVH-MCD curves acquired at 420 nm plotted against $\beta H/2kT$; nearly identical data were obtained at 700 nm. Curves measured at different temperatures do not superimpose, indicating that the $S = 1$ ground state of **1** is subject to a sizable zero-field splitting (ZFS). The appropriate spin Hamiltonian including the Zeeman splitting is then given by eq 3:

$$\mathcal{H} = D[S_z^{\,2} - S(S+1)/3] + E(S_x^{\,2} - S_y^{\,2}) + \mathbf{S}\mathbf{g}\beta\mathbf{H} \tag{3}$$

where D and E are the axial and rhombic ZFS parameters, respectively.[49] The MCD theory for $S > {}^1/_2$ systems describing the relationship between the spin Hamiltonian parameters, the MCD C-term saturation behavior, and the transition polarizations was recently developed by Neese and Solomon.[50] According to this theory, the VTVH-MCD saturation behavior depends on eight parameters: D, E/D, the three principal g values, and the polarization of the transition, expressed by $\%x$, $\%y$, and $\%z$ contributions. To fit the data, a fixed isotropic g value of 2.20 was used, which is a typical value for Ni^{2+} complexes[51] (also note that varying the g values within reasonable limits was found to have negligible effects on the quality of the fits). D and E/D were then varied systematically in increments of 2.5 cm^{-1} and 0.05, respectively, covering the parameter space defined by $-30 \leq D \leq +30$ cm^{-1} and $0 \leq E/D \leq {}^1/_3$, and for each pair of D and E/D values, the polarization was fit to achieve the closest agreement with the experimental VTVH-MCD curves. The quality of each fit was judged from the χ^2 parameter provided by the Simplex least-squares routine. The resulting D and E/D dependence of χ^2 is shown as a contour plot in Figure S1 (Supporting Information). The global minimum was found to be located along a narrow channel extending from ($D = -15$ cm^{-1}, $E/D = 0.15$) to ($D = -7.5$ cm^{-1}, $E/D = 0.3$); thus, although D cannot be determined with high precision, the rhombic parameter $E = -2.25$ cm^{-1} is well-defined. The best fit was obtained with $D = -8.75$ cm^{-1}, $E/D = 0.25$, and transition moment components of $\%x = 0.5$, $\%y = 4.5$, and $\%z = 95.0$, affording excellent agreement between the experimental and simulated VTVH-MCD curves (Figure 5). Nearly identical results were obtained from simultaneous fits of the 420 and 700 nm VTVH-MCD data sets, indicating that both bands A and E are predominantly z polarized.

B. Computations. To obtain quantitative insight into the electronic structure of **1**, spin-unrestricted DFT calculations were performed on the $S = 1$ ($|M_S| = 1$) ground state of this species. In the published crystal structure of (R,R,S,S)-[Ni(tmc)CH$_3$](BAr′$_4$), one carbon atom of the tmc macrocycle is disordered over two positions.[20] Furthermore, the (BAr′$_4^-$) counterion differs from the triflate anion present in **1**, thus possibly affecting the molecular structure of the [Ni(tmc)CH$_3$]$^+$ complex by alterations in the crystal packing. Therefore, the molecular structure of **1** (see Figure 6a, left) was determined by an unconstrained DFT geometry optimization of the entire (R,R,S,S)-[Ni(tmc)CH$_3$]$^+$ cation. For comparison, a single-point DFT calculation using ADF was performed on the crystal structure geometry. Table S9 (Supporting Information) compares key geometric parameters as well as the DFT computed total energies for the two geometries. Importantly, for the optimized model, the total energy is 7.0 eV lower than for the crystal structure model, which predominantly reflects the disorder prior to optimiza-

---

(45) The ellipticity is defined as the rotation angle associated with the differential absorption of left and right circularly polarized light.

(46) The MCD peak intensity and, hence, the $|\theta|$/OD ratio for band F are somewhat inaccurate because of a sizable contribution from a paramagnetic impurity to this region of the MCD spectrum.

(47) Johnson, M. K. In *Physical Methods in Bioinorganic Chemistry: Spectroscopy and Magnetism*; Que, L., Ed.; University Science Books: Sausalito, CA, 2000; pp 233−285.

(48) The presence of a paramagnetic impurity precluded the analysis of VTVH data collected below 370 nm.

(49) Bencini, A.; Gatteschi, D. *Electron Paramagnetic Resonance of Exchange Coupled Systems*; Springer-Verlag: Heidelberg, Germany, 1990.

(50) Neese, F.; Solomon, E. I. *Inorg. Chem.* **1999**, *38*, 1847−1865.

(51) Carlin, R. L. *Magnetochemistry*; Springer: Heidelberg, Germany, 1986; p 67.

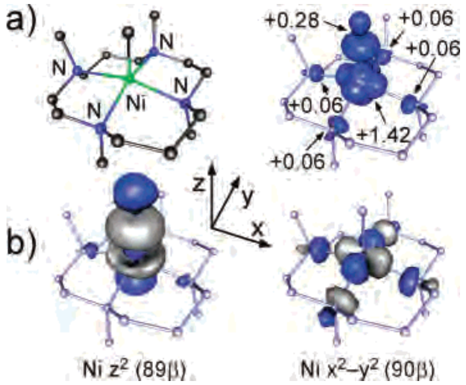

Figure 6. (a) Computational model of **1** (left) and BP DFT-computed total unpaired spin density distribution (right). Unpaired spin densities (isodensity value of 0.01 a.u.) on individual atoms are indicated. (b) Isosurface plots (isodensity value of 0.05 a.u.) of the two Ni 3d-based lowest unoccupied spin-down MOs obtained from a spin-unrestricted BP DFT computation.

tion. Concomitant with the energetic stabilization, the complex became more symmetric upon optimization, nearly adopting C_s symmetry with the pseudo-mirror plane bisecting the Ni, methyl-C, and central methylene C atoms of the six-membered rings located on opposite sides of the macrocyclic ligand (note that for the sake of consistency, we chose to keep the standard orientation of the coordinate system in the parent C_{4v} point group, as shown in Figure 6). However, the average Ni−C and Ni−N bond lengths only increased by 0.025 and 0.04 Å upon optimization, respectively, whereas the average value for ∠(C−Ni−N) decreased marginally from 101.7° to 100.0° (Table S9, Supporting Information). Overall, the differences between the experimental and calculated values for all key bond distances and angles are insignificant; therefore, all subsequent computations were performed on the optimized model of **1** shown in Figure 6a (left).

In an effort to generate an experimentally calibrated electronic structure description of **1**, the TD-DFT method was used to compute a series of absorption spectra for this complex, whereby the amount of Hartree−Fock (HF) exchange added was systematically varied between 0 and 25%. To facilitate comparison with our experimental data, the TD-DFT-predicted transition energies and intensities were used to simulate an absorption spectrum for any given percentage of HF exchange, assuming that each transition gives rise to a Gaussian band with a uniform width of 2600 cm^{-1}, corresponding to the average width of bands A−I (Table 1). Although all TD-DFT computations yielded qualitatively similar results (Figure S2, Supporting Information), the overall best agreement between the experimental and predicted absorption spectra was achieved with the pure BP DFT functional (0% HF exchange). In particular, this latter computation most closely reproduces the experimental observation that three major transitions contribute to the 28 500 cm^{-1} absorption feature (bands F−H, Figure 4 and Table 1). Therefore, the pure BP DFT functional was used in all subsequent analyses and to assign the dominant transitions (Section D). Note, however, that irrespective of the DFT functional chosen, the same general conclusions would be drawn from our computational results.

C. Ground-State Properties. C.1. NCA. To determine the Ni−C bond strength in **1**, a NCA of the corresponding rR data was performed. The fact that the $CH_3 \rightarrow CD_3$ isotopic shift of 28 cm^{-1} for the 463 cm^{-1} mode only slightly deviates from the value of 32 cm^{-1} predicted for an isolated Ni−methyl harmonic oscillator indicates that this mode predominantly involves Ni−C(H$_3$) stretching motion. Thus, to obtain a reasonable value for the Ni−C stretch force constant, it was necessary to consider only the six atoms of the NiN_4C core in our NCA. For these $N = 6$ atoms, there exist $3N - 6 = 12$ vibrational degrees of freedom. To limit the number of force constants and to avoid any redundancy-induced correlations between them, a C_{4v} symmetrized core geometry was used and the N−Ni−N bending modes were omitted, which is justified by the relative rigidity of the tmc macrocycle. The remaining three symmetry-inequivalent internal coordinates are the Ni−C and Ni−N stretching and the C−Ni−N bending coordinates with the corresponding force constants $k_{\mathrm{Ni-C}}$, $k_{\mathrm{Ni-N}}$, and $k_{\mathrm{C-Ni-N}}$, respectively. The Urey−Bradley force field requires an additional force constant k_{UB} for the nonbonded interaction between the N and C atoms. In the C_{4v} point group, the internal coordinates chosen combine to seven normal modes, namely three a$_1$ [ν_{a1}(Ni−C), ν_{a1}(Ni−N), and δ_{a1}(C−Ni−N)], two e [ν_e(Ni−N) and δ_e(C−Ni−N)], and two b$_1$ [ν_{b1}(Ni−N) and δ_{b1}(C−Ni−N)], see Figure S3 in the Supporting Information. The mass of the carbon atom was set to the value for the entire methyl group[52] and was varied accordingly to account for the isotopes CH_3 and CD_3.

Because only the totally symmetric modes can directly couple to electronic transitions and are, thus, expected to be strongly rR enhanced, the 463/435 cm^{-1} and 117/115 cm^{-1} isotope-sensitive modes were assigned to the ν_{a1}(Ni−C) stretching and δ_{a1}(C−Ni−N) bending modes, respectively. Because either the 232 cm^{-1} or the 348 cm^{-1} feature could be assigned to the remaining totally symmetric mode [i.e., the Ni−N breathing mode ν_{a1}(Ni−N)], both possibilities were considered in two independent NCAs. Initial estimates of $k_{\mathrm{Ni-C}} = 1.0$ mdyn/Å, $k_{\mathrm{Ni-N}} = 0.5$ mdyn/Å, and $k_{\mathrm{C-Ni-N}} = 0.25$ mdyn Å/rad^2 were used, whereas the value for the Urey−Bradley nonbonding interaction was set to $k_{\mathrm{UB}} = 0.05$ mdyn/Å. The force constants $k_{\mathrm{Ni-C}}$, $k_{\mathrm{Ni-N}}$, and $k_{\mathrm{C-Ni-N}}$ were then fitted to achieve the best agreement between the experimental and calculated vibrational frequencies.

The calculated frequencies obtained with the fitted force constants agree very well with the experimental values for both assignments of the ν_{a1}(Ni−N) mode to either the 232 cm^{-1} (Table 2) or the 348 cm^{-1} rR feature (Table S10, Supporting Information). On the other hand, fits with the 232 and 348 cm^{-1} features assigned to different Ni−N stretches yielded poor agreement between predicted and observed frequencies (not shown), suggesting that one of them does not correspond to a fundamental but rather to a combination or overtone mode. Indeed, the value of 348 cm^{-1} is consistent with it being the sum of the frequencies of the

---

(52) The C−H vibrations occur at much higher frequencies because of the low mass of the hydrogen atoms and are, therefore, decoupled from the vibrations of the NiN_4C framework.

Table 2. Experimental and Calculated Vibrational Frequencies for **1** with the 232 cm^{-1} Mode Assigned to ν_{a1}(Ni−N)[a]

		exptl freqs		NCA		
normal mode	sym	CH_3	CD_3	CH_3	CD_3	force constants
ν_{a1}(Ni−C)	a_1	463	435	463	431	$k_{Ni-C} = 1.44$
ν_e(Ni−N)	e			272	272	
ν_{a1}(Ni−N)	a_1	232	232	232	232	$k_{Ni-N} = 0.40$
ν_{b1}(Ni−N)	b_1			227	227	
δ_e(C−Ni−N)	e			172	164	
δ_{a1}(C−Ni−N)	a_1	117	115	117	116	$k_{C-Ni-N} = 0.22$ (0.05)[b]
δ_{b1}(C−Ni−N)	b_1			90	90	

[a] Calculated values were obtained from a NCA of the $NiCN_4$ unit. Frequencies are given in cm^{-1}, and stretching and bending force constants *k* are given in mdyn/Å and mdyn Å/rad^2, respectively. [b] Urey−Bradley nonbonding interaction constant in mdyn/Å.

117/115 cm^{-1} and 232 cm^{-1} modes; therefore, the 348 cm^{-1} mode is assigned as the combination band associated with the totally symmetric Ni−N stretching and C−Ni−N bending modes.[53] This assignment is corroborated by the low rR intensity of the 348 cm^{-1} mode compared to those of both the 117/115 and 232 cm^{-1} modes. Note that the alternative assignment of the 348 cm^{-1} mode to ν_{a1}(Ni−N) would require the 232 cm^{-1} mode to correspond to the first overtone of the 117/115 cm^{-1} bend, 2δ_{a1}(C−Ni−N), which can be ruled out on the basis of the relative rR intensities of these two modes (Figure 3) and the lack of any discernible isotope shift of the 232 cm^{-1} mode.

Our NCA reveals that the fitted force constant for the Ni−C stretch, $k_{Ni-C} = 1.44$ mdyn/Å, is virtually independent from the assignments of the other modes. This result is a direct consequence of the fact that the ν_{a1}(Ni−C) mode involves predominantly (95%) Ni−C stretching motions and negligible (0.1%) Ni−N stretching motions, as revealed by the potential energy distribution (PED) contributions listed in Table 3 and Table S11 in the Supporting Information. On the other hand, the ν_{a1}(Ni−N) and δ_{a1}(C−Ni−N) normal modes both possess substantial contributions from the Urey−Bradley nonbonding interaction of 9% and 26%, respectively, and the latter mode also involves about 5% Ni−N stretching motion (Table 3). These results reveal that the C−Ni−N bending and Ni−N stretching motions are strongly coupled, which likely accounts for the large intensity of the δ_{a1}(C−Ni−N) mode in the rR spectra of **1** in Figure 3. The fact that the ν_{a1}(Ni−N) mode gives rise to the most intense feature in rR spectra obtained with 407 nm (24 588 cm^{-1}) excitation indicates that the corresponding transition also carries substantial N → Ni CT character (see Section D for band assignments).

C.2. Nature of Ni−Ligand Bonding. One of the main objectives of this study was to obtain quantitative insight into the nature of the Ni−C bond in **1**. To accomplish this goal, the DFT method was used in conjunction with the BP functional that was chosen for reasons outlined in Section B. Figure 6a (right) shows the distribution of the total unpaired spin density, whereas Table 4 lists the energies and compositions of the relevant Ni 3d- and C and N 2p-based MOs, as obtained from BP DFT computations on the geometry-optimized model of **1** (note that although the physical relevance of MOs obtained from DFT computations is a matter of dispute, the computed electron density is directly related to the experimentally observable spin density). In the $S = 1$ ground state of **1**, the two unpaired electrons occupy the Ni z^2- and $x^2 - y^2$-based MOs 90α and 89α, respectively.[54] As a result of spin polarization, these MOs are strongly stabilized by 1.342 and 1.913 eV relative to their unoccupied spin-down counterparts 89β and 90β, respectively (Table 4). This spin polarization also leads to a stabilization of the other Ni 3d-based spin-up MOs relative to their spin-down counterparts, albeit to a lesser extent.

The Ni−ligand bonding interactions are best inferred from the Ni 3d-based unoccupied MOs that are σ antibonding with respect to the methyl C-based and tmc N-based frontier orbitals (Figure 6b). Consequently, the dominant Ni−C bonding interaction involves the Ni z^2 and C p_z orbitals forming the Ni−C σ antibonding MO 89β (Table 4). The large methyl C p_z orbital contribution to MO 89β, which is particularly evident from the corresponding isosurface plot (Figure 8), indicates that the Ni−C bond is highly covalent in nature. Because MO 89β is unoccupied, its large C p_z orbital character reflects a substantial degree of C → Ni electron delocalization in the occupied Ni−C σ bonding counterpart (MO 85β). This bonding description implies that the Ni−C bond has considerable $Ni^+/CH_3^{\bullet}$ biradical character, which is consistent with the substantial delocalization of the computed total unpaired spin density over the Ni−C bond (Figure 6a). The dominant Ni−N bonding interactions involve the Ni $x^2 - y^2$ orbital and the N p_x, p_y-based lone pairs that are the main contributors to the σ antibonding MO 90β (Table 4). As evidenced by the isosurface plots of this MO and the total unpaired spin density in Figure 6, the Ni−N bonds are substantially less covalent than the Ni−C bond.

C.3. Spin Hamiltonian Parameters. To corroborate the spin Hamiltonian parameters (eq 3) for the $S = 1$ ground state of **1** obtained from the VTVH-MCD data analysis (Section A.2), semiempirical INDO/S-CI calculations were performed on the DFT optimized model of **1** as described in the Experimental Methods section. However, even on approaching the maximum number of configurations manageable by ORCA, no stable values for the ZFS parameters and *g* values were obtained (i.e., small variations in the number of excited configurations included consistently led to substantial changes in the computed spin Hamiltonian parameters). This instability possibly reflects the presence of low-lying LF excited states, predicted by INDO/S-CI computations at ∼4500 cm^{-1}, which may preclude the use of perturbation theory to compute accurate spin Hamiltonian parameters. However, approximate values of $D = -5$ to -8 cm^{-1} and $E/D \approx 0.1$ and an essentially isotropic *g* tensor with $g_x \approx g_y \approx g_z \approx 2.20$ can be derived from our INDO/S-CI computations. These values are consistent with the results from the analysis of our VTVH-MCD data, in particular, with respect to the sign of *D* (see Section A.2)

---

(53) The isotopic shift of the 348 cm^{-1} mode of 1−2 cm^{-1} that would be expected on the basis of this assignment lies within the experimental error of the frequencies determined from our rR data.

(54) Throughout the manuscript, Ni 3d orbitals are labeled using an abbreviated notation (e.g., *xy* stands for $3d_{xy}$).

Table 3. Normal Mode Descriptions for the NiCN$_4$ Unit of **1-CH$_3$** with the 232 cm^{-1} Mode Assigned to ν_{a1}(Ni−N)

		eigenvectors[a]			PED[b]			
normal mode	sym	Ni−C	Ni−N	C−Ni−N	Ni−C	Ni−N	C−Ni−N	UB[c]
ν_{a1}(Ni−C)	a$_1$	+0.289	−0.007	−0.025	94.9	0.1	0.5	4.6
ν_{e}(Ni−N)	e	0.000	±0.185/±0.134	∓0.038/∓0.027	0.0	94.6	2.2	3.2
ν_{a1}(Ni−N)	a$_1$	−0.006	+0.134	+0.018	0.2	89.8	0.9	9.1
ν_{b1}(Ni−N)	b$_1$	0.000	±0.133	±0.003	0.0	92.6	0.0	7.4
δ_{e}(C−Ni−N)	e	0.000	±0.005/±0.006	∓0.103/∓0.125	0.0	0.2	66.5	33.3
δ_{a1}(C−Ni−N)	a$_1$	+0.003	+0.016	−0.078	0.1	5.4	68.3	26.2
δ_{b1}(C−Ni−N)	b$_1$	0.000	±0.008	∓0.061	0.0	2.3	68.6	29.1

[a] Mass-weighted eigenvectors $\mathbf{L}_n$. [b] PED in %. [c] Urey−Bradley nonbonded interaction.

Table 4. Energies (in eV) and Compositions of the Ni 3d-Based and Relevant Ligand-Based Molecular Orbitals Obtained from a Spin-Unrestricted Pure DFT Calculation on **1**[a]

Spin-Up MOs

				Ni					C(H$_3$)	N	C, H
#	MO[b]	*E* (eV)	occ[c]	*xy*	*xz*	*yz*	z^2	$x^2 - y^2$	p$_z$	tot	tot
90α	z^2	−6.963	1	0	0	0	29	0	41	6	6
89α	$x^2 - y^2$	−7.370	1	0	0	0	0	48	0	34	14
88α	*yz*	−8.258	1	1	34	53	0	0	0	5	4
87α	*xz*	−8.284	1	0	52	32	0	1	0	6	6
86α	*xy*	−8.532	1	95	0	0	0	1	0	1	2
85α	N p$_{x/y}$	−9.733	1	0	6	5	0	0	0	44	37
84α	C p$_z$	−9.964	1	0	0	0	54	0	26	6	7
83α	N p$_{x/y}$	−10.032	1	0	3	4	5	0	4	46	29
82α	N p$_{x/y}$	−10.613	1	0	0	0	0	46	0	20	32

Spin-Down MOs

				Ni					C(H$_3$)	N	C, H
#	MO[b]	*E* (eV)	occ[c]	*xy*	*xz*	*yz*	z^2	$x^2 - y^2$	p$_z$	tot	tot
90β	$x^2 - y^2$	−5.457	0	1	0	0	1	73	0	15	6
89β	z^2	−5.621	0	0	0	0	49	1	23	4	6
88β	*yz*	−7.519	1	0	37	54	0	0	0	5	3
87β	*xz*	−7.561	1	0	53	36	0	0	0	4	4
86β	*xy*	−7.834	1	96	0	0	0	1	0	1	2
85β	C p$_z$	−8.677	1	0	0	0	42	0	44	2	4
84β	N p$_{x/y}$	−9.563	1	0	3	3	0	0	0	48	37
83β	N p$_{x/y}$	−9.778	1	0	0	0	0	23	0	47	34
82β	N p$_{x/y}$	−9.869	1	0	2	2	0	0	0	51	32

[a] Only Ni 3d, N 2p, and methyl-C 2p$_z$ orbital contributions are shown. [b] MOs are labeled according to the atomic orbitals that produce the dominant contribution.[58] [c] Occupation number.

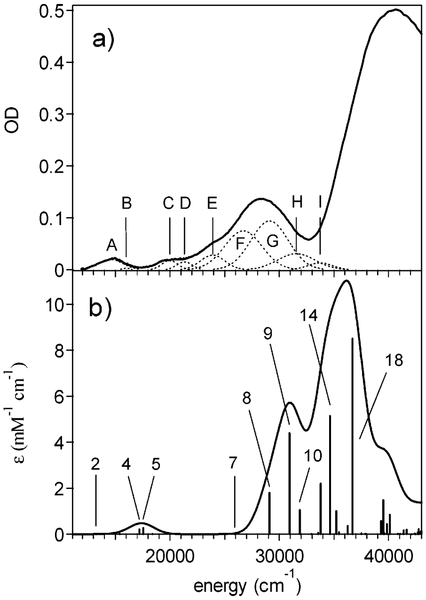

Figure 7. Experimental 4 K (a) and BP TD-DFT calculated (b) absorption spectra of **1**. The labeling scheme for the experimental transitions relates to Figure 4 and Table 1. Transitions producing the dominant contributions to the calculated spectrum are indicated by vertical lines. The numbering scheme used to label excited states relates to Table 5.

D. Excited States. D.1. TD-DFT Calculations. The spectral analysis presented in Section A.2 reveals that at least nine electronic transitions contribute to the spectral region between 12 000 and 35 000 cm^{-1} (labeled A−I in Figures 4 and 7a and Table 1). Bands A−E and I are assigned to LF transitions on the basis of their low absorption intensities and large $|\theta|$/OD ratios (Table 1), whereas bands F−H, as well as the dominant absorption feature at 40 500 cm^{-1}, are attributed to CT transitions. To identify the donor and acceptor orbitals involved in these transitions, the results from the BP TD-DFT calculation on **1** (Section B) will be used in the following.

The computed absorption spectrum for **1** exhibits 18 transitions below 37 000 cm^{-1} (Figure 7b); the energies, oscillator strengths, molecular polarizations, and principal donor and acceptor MOs of the relevant transitions are listed in Table 5. Three dominant transitions can be identified at 30 920, 34 640, and 36 690 cm^{-1} that are labeled 9, 14, and 18, respectively, in Figure 7. Transition 9 primarily involves C p$_z$ (85β) → Ni z^2 (89β) one-electron excitation (Table 5 and Figure 8). The C → Ni CT character of this transition is particularly evident from the corresponding EDDM (Figure 9), which shows that, upon excitation, substantial electron density is transferred from C to Ni, giving rise to a transition moment that is oriented along the Ni−C bond vector (i.e., parallel to the molecular *z* axis). Transitions 14 and 18 essentially correspond to the one-electron excitations from the N p$_x$, p$_y$-based MOs 84β and 82β, respectively, to the Ni $x^2 - y^2$-based MO 90β. The N → Ni CT character of these transitions is also apparent from the corresponding EDDMs (Figure 9) and is consistent with the fact that their transition moments are oriented perpendicular to the molecular *z* axis (Table 5).

D.2. Spectral Assignments. Figure 7 reveals that the prominent bands at 28 500 and 40 500 cm^{-1} in the experimental absorption spectrum of **1** are reasonably well-reproduced by the TD-DFT computation, which predicts two similar features associated with transitions 9 and 14/18, respectively. On the basis of the results presented in the preceding section, we may, thus, conclude that the bulk of the intensity of the 28 500 and 40 500 cm^{-1} band systems arises from C p$_z$ → Ni z^2 and N p$_x$, p$_y$ → Ni $x^2 - y^2$ CT

Table 5. TD-DFT Calculated Energies ν_{calc} (in cm^{-1}), Oscillator Strengths f, Molecular Polarizations (in %), and Percent Contributions from Dominant One-electron Excitations of Relevant Transitions[58]

band[a]	ν_{max}[a]	state	ν_{calc}	f	%x	%y	%z	one-electron excitation	%
A	14 560	2	13 240	0.000 01	20.1	79.0	0.9	Ni xz (87β) → Ni z^2 (89β)	66
B	16 000							spin flip	
C	19 980	4	17 200	0.002 43	11.3	88.7	0.0	Ni yz (88β) → Ni x^2-y^2 (90β)	64
D	21 325	5	17 544	0.003 25	80.7	19.3	0.0	Ni xz (87β) → Ni x^2-y^2 (90β)	76
E	23 900	7	25 917	0.000 10	27.5	33.6	38.9	C p$_z$ (85β) → Ni x^2-y^2 (90β)	97
								C p$_z$ (85β) → Ni z^2 (89β)	2
F	26 700	8	29 106	0.021 56	0.1	0.2	99.7	Ni z^2 (90α) → Ni p$_z$(91α)	89
								C p$_z$ (85β) → Ni z^2 (89β)	9
G	29 100	9	30 920	0.052 78	0.2	0.1	99.7	C p$_z$ (85β) → Ni z^2 (89β)	63
								N p$_x$, p$_y$ (83β) → Ni x^2-y^2 (90β)	19
H	31 550	10	31 861	0.012 64	70.1	29.9	0.0	N p$_x$, p$_y$ (84β) → Ni z^2 (89β)	98
I	33 740	12	33 554	0.000 63	98.1	0.3	1.6	N p$_x$, p$_y$ (83β) → Ni z^2 (89β)	97
		13	33 778	0.026 35	38.6	61.1	0.3	N p$_x$, p$_y$ (84β) → Ni x^2-y^2 (90β)	68
								N p$_x$, p$_y$ (82β) → Ni z^2 (89β)	28
	∼40 500	14	34 640	0.061 76	53.4	46.0	0.6	N p$_x$, p$_y$ (82β) → Ni z^2 (89β)	68
								N p$_x$, p$_y$ (84β) → Ni x^2-y^2 (90β)	23
	∼40 500	18	36 690	0.102 21	48.9	51.1	0.0	N p$_x$, p$_y$ (82β) → Ni x^2-y^2 (90β)	91

[a] Experimental band positions (in cm^{-1}) from the Gaussian deconvolution of the absorption and MCD spectra of **1** (Figure 4 and Table 1).

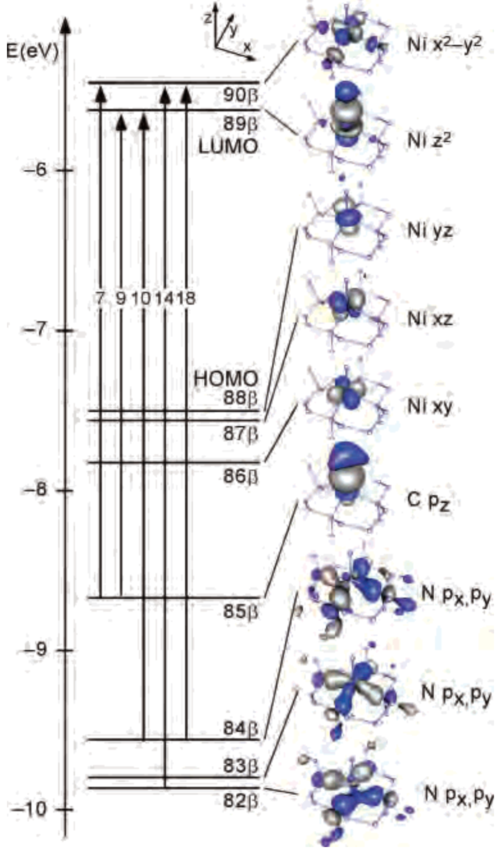

Figure 8. Energy level diagram showing the key spin-down canonical MOs obtained from a spin-unrestricted BP DFT computation on **1**. Isosurface plots (isodensity value of 0.05 a.u.) of the MOs are shown on the right. MOs are labeled according to their main contributors. The arrows indicate the dominant one-electron excitations involved in key CT transitions based on the TD-DFT computation on **1** (see Table 5 for numbering scheme used).

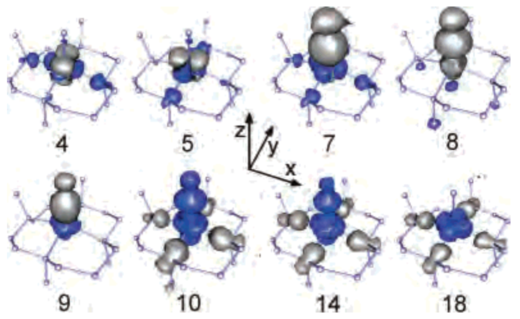

Figure 9. Electron density difference maps (EDDMs; isodensity value of 0.005 a.u.) for selected transitions (see Table 5 for numbering scheme used). Grey and blue indicate a loss and gain of electron density, respectively.

transitions, respectively. Because transition 9 also contains a 19% contribution from the N p$_x$, p$_y$ (83β) → Ni x^2-y^2 (90β) one-electron excitation (Table 5),[55] our computations predict that the 28 500 cm^{-1} band possesses both C → Ni and N → Ni CT character. This prediction is consistent with the experimental finding that both the Ni−C and Ni−N stretching modes ν_{a1}(Ni−C) and ν_{a1}(Ni−N), respectively, are enhanced in rR spectra obtained upon excitation in resonance with this feature (Figure 3). The mixed character transition 9 presumably stems from CI mixing of the C p$_z$ → Ni z^2 and N p$_x$, p$_y$ → Ni x^2-y^2 CT excited states, because TD-DFT computations employing the B3LYP hybrid functional, which overestimate the energy separation between the C → Ni and N → Ni CT excited states (Figure S2, Supporting Information), predict that the corresponding transition has negligible N → Ni CT character.

Our Gaussian deconvolution reveals that the experimental absorption band at 28 500 cm^{-1} possesses contributions from the three transitions F−H (Figure 7a; Section A.2). Similarly, the TD-DFT-computed spectrum also exhibits three transitions in this region, including transitions 8 and 10 at 29 106 and 31 861 cm^{-1}, respectively, along with the C p$_z$ → Ni z^2 CT transition 9 discussed above (Figure 7b). Consequently, bands F and H may be attributed to transitions 8 and 10, respectively.[56] Transition 8 primarily involves one-electron excitation from the Ni z^2-based MO 90α to a Ni-based orbital (MO 91α) reminiscent of a 4sp^2 hybrid. The large (47%) C

---

(55) This contribution to transition 9 is not evident from the EDDM in Figure 9, but it becomes obvious if a lower isodensity value (0.002 a.u.) is employed.

(56) An alternative assignment of bands G−I to vibrational sidebands of the electronic transition F can be ruled out because the energy spacing between bands F−I of ∼2000 cm^{-1} far exceeds the frequency of any resonance enhanced vibrational mode in the rR spectra obtained with laser excitation in this spectral region (Figure 3).

p_z orbital contribution to the donor MO (Table 4) along with the 9% contribution from the C p_z (85β) → Ni z^2 (89β) excitation (Table 5) orient the corresponding transition dipole moment along the Ni−C bond vector (Table 5; also see EDDM in Figure 9). Transition 10 corresponds to the N p_x, p_y (84β) → Ni z^2 (89β) CT excitation (Table 5).

Band E at 23 900 cm^{-1}, which dominates the MCD spectrum, is assigned to the TD-DFT calculated transition 7 at 25 917 cm^{-1}. Although this transition formally corresponds to the C p_z (85β) → Ni $x^2 - y^2$ (90β) CT excitation, it carries substantial LF character because of the large (44%) contribution from the Ni z^2 orbital to the donor MO (Table 5), consistent with the high $|\theta|$/OD ratio observed experimentally. The corresponding EDDM plot (Figure 9) indicates that electron density is predominantly transferred along the Ni−C bond vector, in excellent agreement with the results from our VTVH-MCD data analysis.[57]

Bands C, at 19 980 cm^{-1}, and D, at 21 325 cm^{-1}, are assigned to the Ni *yz* (88β) → Ni z^2 (89β) transition 4 predicted at 17 200 cm^{-1} and the Ni *xz* (87β) → Ni z^2 (89β) transition 5 at 17 544 cm^{-1}, respectively.[58] Support for this assignment is provided by the MCD spectra in Figure 4b, where these two LF transitions give rise to a derivative-shaped pseudo-A term feature. MCD intensity requires the presence of two perpendicularly polarized transition dipole moments. Although **1** does not possess orbitally degenerate states because of its low symmetry, this requirement can be fulfilled through mixing between the ground state and excited states or among excited states via spin−orbit coupling. In situations where spin−orbit coupling between a pair of energetically proximate excited states becomes dominant, the corresponding MCD transitions will be equally intense but oppositely signed, leading to the appearance of a derivative-shaped pseudo-A term feature. Consequently, observation of a pseudo-A term associated with bands C and D (Figure 4b) requires the corresponding transition moments to be mutually orthogonal, which is indeed the case for transitions 4 and 5, which are polarized mainly along *y* and *x*, respectively (Table 5; also see EDDMs in Figure 9).

TD-DFT-assisted tentative assignments of the remaining features in the absorption and MCD spectra of **1** (Figure 4) are also included in Table 5.[59] Note that band B at 16 000 cm^{-1}, assigned in Section A.2 to a spin-flip transition on the basis of its narrow width, is not predicted by the TD-DFT calculation because this method only considers electronic excitations within the same spin manifold. However, the semiempirical INDO/S-CI calculation predicts this transition at 12 460 cm^{-1}, in fair agreement with the experimental results.

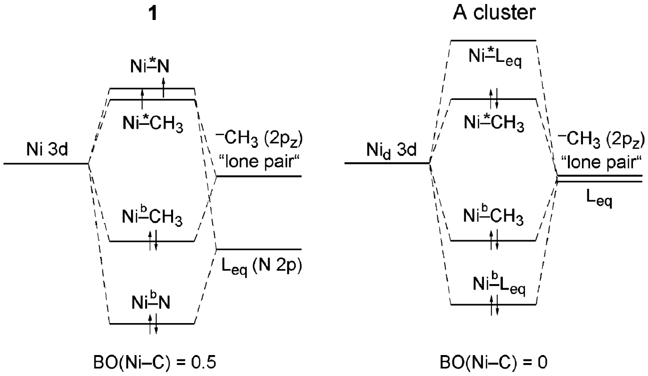

Figure 10. Schematic illustration of the Ni−ligand bonding interactions in **1** and the methylated Ni_d center of a hypothetical A cluster model. Bonding (b) and antibonding (*) interactions are indicated. L_{eq} denotes the equatorial ligand atoms.

In summary, our TD-DFT-assisted spectral analysis reveals that the electronic absorption spectrum of **1** can be divided into three major regions, as indicated in Figure 2: region I contains mainly LF transitions, whereas regions II and III are dominated by C → Ni and N → Ni CT transitions, respectively. Importantly, the good agreement between the experimental and calculated absorption spectra lends credence to our computed bonding description for **1** and warrants the use of the BP DFT method to explore Ni−CH_3 bonding in hypothetical A cluster models, as discussed below.

Discussion

Ni−Methyl Bonding in $[Ni(tmc)CH_3]^+$ (1). Our experimentally calibrated DFT computations allow for substantial insight into the nature of Ni−CH_3 bonding in complex **1**. As illustrated in Figure 10 (left), the close energetic proximity of the C p_z-based frontier orbital of the methyl group and the Ni 3d orbitals gives rise to an extremely covalent Ni−C bond and, consequently, to a large splitting between the C p_z-based σ bonding MO and its Ni z^2-based σ antibonding counterpart. Therefore, the latter MO is energetically close to the Ni $x^2 - y^2$-based Ni−N σ antibonding MO, despite the fact that **1** is only five-coordinate, possessing a single axial ligand. The resulting energy separation of ~0.5 eV between these two MOs is considerably smaller than the spin pairing energy of ~2.0 eV estimated from the energy of the spin-flip transition B in Figure 4, and **1**, thus, adopts a high-spin ($S = 1$) ground state. As a result, the σ antibonding Ni z^2-based MO is only singly occupied, leading to a formal Ni−C bond order of 0.5. To evaluate the impact of the Ni^{2+} spin state on Ni−C bonding, a spin-restricted (i.e., $S = 0$) DFT calculation on a hypothetical low-spin model of **1** was attempted. However, convergence of the wave function required complete removal of the methyl group (model **1b**), demonstrating that the strong σ donor ability of the methyl ligand and the consequent stabilization of a high-spin Ni^{2+} ground state are essential prerequisites for Ni−C bond formation in the preparation of **1**.

---

(57) The computed *xy* polarization of transition 7 (Table 5) reflects the high N p_x, p_y orbital character of the principal acceptor MO (90β).

(58) Because of the coordinate system chosen, the Ni *xz* and *yz* orbitals in **1** are strongly mixed; the designations *xz* and *yz* are, thus, used solely for labeling purposes.

(59) Band A at 14 560 cm^{-1} is tentatively assigned to transition 2, predicted at 13 240 cm^{-1}, which is mainly due to the Ni *xz* (87β) → z^2 (89β) excitation on the basis of its EDDM (not shown). This EDDM also suggests the presence of a substantial transition dipole moment along the Ni−C bond, in agreement with the *z* polarization of band A as deduced from the VTVH-MCD data analysis (Section A.2). Band I at 33 740 cm^{-1} is assigned to the N p_x, p_y (83β) → Ni z^2 (89β) CT transition 12 at 33 554 cm^{-1}, which is predicted to carry only little absorption intensity because of the vastly different compositions of the donor and acceptor MOs, in agreement with our experimental data.

Methyl-Binding Site of the ACS A Cluster. As demonstrated in this study, the BP DFT method provides an accurate Ni$-$C bonding description for **1** and, thus, appears well-suited to evaluate hypothetical models of the methylated A cluster. Although circumstantial[15] and computational[11] evidence suggest that Ni_p is the site of methyl binding, it has also been proposed that the methyl transfer from the $CH_3$$-$CoFeSP protein to the ACS A cluster involves the distal Ni center (Ni_d) while CO binds to the proximal center (Ni_p),[5,16,17] thereby invoking a binuclear mechanism for ACS catalysis. To evaluate the likelihood of methyl binding to Ni_d, DFT computations were performed on hypothetical models of the oxidized A cluster possessing an axially bound methyl group on Ni_d and lacking the $[Fe_4S_4]$ unit, $[\{S(CH_3)_2\}Ni_p^{2+}Ni_d^{2+}-CH_3]$ (Chart 1).[60] Both $S = 1$ (model **2a**) and spin-restricted $S = 0$ (model **2b**) A cluster states were investigated with initial Ni$-$C bond lengths of 2.0 and 2.5 Å, respectively.[61] The total energies and unpaired spin densities of these and all other models discussed in the text are listed in Table S12 in the Supporting Information. Interestingly, model **2a** converged to an $S = {}^1/_2$ $Ni_d^{3+}-CH_3$ species ferromagnetically coupled to an $S = {}^1/_2$ Ni_p^+ center, $[\{S(CH_3)_2\}Ni_p^+Ni_d^{3+}-CH_3]$. Upon subsequent geometry optimization of this mixed-valence species, the methyl group spontaneously transferred from the distal to the proximal Ni center (which, therefore, adopted a tetrahedral geometry to ensure a high-spin ground state as required by the $S = 1$ total spin imposed on this model), yielding $[\{S(CH_3)_2\}Ni_p^{2+}-CH_3Ni_d^{2+}]$ (model **3a**, Chart 1), with the unpaired spin density now mainly residing on Ni_p (Table S12, Supporting Information). Similarly, the diamagnetic A cluster model **2b** underwent spontaneous methyl transfer from Ni_d to Ni_p upon geometry optimization, yielding **3b** (Chart 1).

These results strongly suggest that methylation of the A cluster occurs at Ni_p rather than Ni_d. This preference can be understood by comparing metal$-$ligand bonding in **2a** and **1**, because both species possess similar square-pyramidal $Ni-CH_3$ core structures. As shown in the previous section, the formation of a stable axial Ni$-$C bond in such square-pyramidal complexes can only occur if the Ni^{2+} adopts a high-spin electron configuration, which requires the Ni 3d-based Ni$-$C and $Ni-L_{eq}$ σ antibonding MOs (where L_{eq} denotes the equatorial ligands) to be in close energetic proximity (Figure 10). Consequently, the axial Ni$-$C bond strength critically depends on the electronic properties of the equatorial ligands. As illustrated in Figure 10, the equatorial LF experienced by Ni_d in the A cluster is much stronger than that associated with the tmc ligand in **1** as a result of the presence of two deprotonated amides. This difference leads to a considerably larger destabilization of the Ni_d-L_{eq} σ antibonding MO in the protein than it does in **1** and, thus, leads to the inability of Ni_d^{2+} to adopt the high-spin ground-state necessary for the formation of a stable Ni$-$C bond.

Table 6. Comparison of $M-CH_3$ Bond Orders and Stretch Force Constants k_{M-C} (in mdyn/Å) for **1**, **3a**, **4**, and **5**

	1	**3a**	**4**	**5**
BO[a]	0.848	0.944	1.038	1.136
k_{M-C}	1.44[b]	1.60[c]	1.76[c]	1.85[d]

[a] Löwdin bond orders as obtained from single-point DFT computations using ORCA. [b] From the NCA of our rR data of **1** (see Section C.1). [c] Estimated from the computed bond orders and $k_{Ni-C} = 1.44$mdyn/Å for **1**. [d] From ref 62.

Comparison of $Ni^{2+}-C$ and $Co^{3+}-C$ Bonding. To further our understanding of the fascinating methyl transfer reaction from the $CH_3$$-$CoFeSP protein to the A cluster (eq 2), it is instructive to compare the Ni_p-C and Co$-$C stretch force constants and bond orders, as both provide a measure of the corresponding bond strengths. The corrinoid cofactor in $CH_3$$-$CoFeSP is methylcobinamid ($MeCbi^+$), for which a Co$-$C stretch force constant of $k_{Co-C} = 1.85$ mdyn/Å has been reported.[62] This value is considerably larger than the Ni$-$C stretch force constant of $k_{Ni-C} = 1.44$ mdyn/Å determined for **1**, indicating a stronger metal$-$methyl bond in the $MeCbi^+$ cofactor. To estimate the Ni$-$C bond strength in the methylated A cluster, the Ni$-$C bond orders for viable A cluster models possessing a methylated proximal Ni_p^{2+} center were calculated using the DFT method. The two structures considered include model **3a** featuring a tetrahedrally coordinated $S = 1$ Ni_p^{2+} center (vide supra) and model **4** possessing a square-planar $S = 0$ Ni_p^{2+} center (Chart 2).[60]

The calculated Ni$-$C bond orders in **3a** and **4** are 11% and 22% higher than in **1**, respectively (Table 6). An analysis of the key MOs of these models indicates that in **3a**, the Ni$-$C σ antibonding MO is singly occupied, as in **1**, whereas in **4**, it is empty (Figure S4). Because the Ni$-$C σ bonding MO is doubly occupied in all cases, this leads to an increase in the formal bond order from 0.5 for **1** and **3a** to 1.0 for **4**.[63] To validate our assumption that calculated metal$-$carbon bond orders (Table 6) provide a reasonable measure of the corresponding bond strengths, we also computed the Co$-$C bond order for $MeCbi^+$ (model **5**, Chart 3). Indeed, the ratio of computed bond orders for **1** and **5**, BO(Ni$-$C, **1**)/BO(Co$-$C, **5**) = 0.75, agrees nicely with the ratio of experimental force constants, $k_{Ni-C}/k_{Co-C} = 0.78$, as well as the ratio of experimentally determined M$-$C(benzyl) bond dissociation energies,[64] BDE(Ni$-$C, **1**)/BDE(Co$-$C, MeCbl) = 0.83. When the ratio BO(Ni$-$C, **3a**)/BO(Ni$-$C, **1**) = 1.11

---

(60) See Experimental Methods for details. The $[Fe_4S_4]^{2+}$ unit had to be omitted to allow for spin-restricted calculations. For consistency, truncated A cluster models were used throughout this study. This truncation is not problematic because the $[Fe_4S_4]$ unit is in the diamagnetic +2 oxidation state before and after methylation of the A cluster.

(61) With Ni$-$C bond lengths below 2.5 Å, model **2b** failed to converge.

(62) (a) Dong, S.; Padmakumar, R.; Banerjee, R.; Spiro, T. *J. Am. Chem. Soc.* **1996**, *118*, 9182$-$9183. (b) Dong, S.; Padmakumar, R.; Banerjee, R.; Spiro, T. *Inorg. Chim. Acta* **1998**, *270*, 392$-$398.

(63) The discrepancies between formal and DFT-computed bond orders mainly arise from the fact that the former neglect contributions from the Ni 4s and 4p orbitals to bonding.

(64) Although the $Ni-CH_3$ bond dissociation energy (BDE) for **1** is not available, it is useful to compare the M$-$C BDEs for the benzyl (Bn) derivative of **1** and benzylcobalamin (BnCbl). In BnCbl, the Co$-$C BDE is 23(1) kcal/mol (Brown, K. L.; Brooks, H. B. *Inorg. Chem.* **1991**, *30*, 3420$-$3430), whereas in $[Ni(tmc)Bn]^+$, the Ni$-$C BDE is 19(1) kcal/mol (Schofield, M. H.; Halpern, J. *Inorg. Chim. Acta* **2003**, *345*, 353$-$358).

and our experimentally determined value of $k_{\mathrm{Ni-C}} = 1.44$ mdyn/Å for **1** are used, a value of $k_{\mathrm{Ni-C}} = 1.60$ mdyn/Å may, therefore, be estimated for the Ni−C bond in **3a**. When the same approach is followed, a value of $k_{\mathrm{Ni-C}} = 1.76$ mdyn/Å is predicted for **4**. A comparison of the total energies of the tetrahedral (**3a)** and square-planar (**4)** models (Table S12, Supporting Information) indicates that the latter is energetically favored by 0.34 eV (7.8 kcal/mol) over the former. Additionally, an analysis of the crystal structure of the "open" ACS conformation in which the CH_3−CoFeSP protein can access the A cluster reveals that a square-planar Ni_p site is also favored on the basis of steric considerations.[5,6] Collectively, these results suggest that the methyl-bound Ni_p^{2+} center in the A cluster adopts a square-planar ($S = 0$) rather than a tetrahedral ($S = 1$) conformation, consistent with the fact that the latter structure is unprecedented in the extensive organonickel literature.[65] Importantly, the value of $k_{\mathrm{Ni-C}} = 1.76$ mdyn/Å for **4** is very close to the value of $k_{\mathrm{Co-C}} = 1.85$ mdyn/Å reported for MeCbi^+,[62] suggesting that the organometallic bonds in the methylated A cluster and in CH_3−CoFeSP are similarly strong. Although this similarity alone does not ensure reversible methyl transfer from CH_3−CoFeSP to Ni_p, it may play a key role in balancing the thermodynamics of this reaction.[66]

Conclusions

The spectroscopic and computational studies on the $[\mathrm{Ni(tmc)CH_3}]^+$ complex **1** reported herein provide a quantitative description of Ni−CH_3 bonding in this species, revealing an extremely covalent Ni−C bond with partial $\mathrm{Ni}^+/\mathrm{CH_3}^\bullet$ biradical character. Application of our experimentally calibrated DFT methodology to the study of hypothetical methylated A cluster models leads to the conclusion that methyl binding to the distal Ni center is precluded for electronic reasons, because the strong equatorial LF generated by the deprotonated amides prevents Ni_d^{2+} from adopting a high-spin electron configuration, resulting in a formal Ni_d−C bond order of zero. On the other hand, the lower coordination number of Ni_p relative to that of Ni_d permits the methyl group to bind equatorially, thus allowing for the formation of a stable, square-planar (low-spin) Ni_d^{2+}−CH_3 adduct. Collectively, these results provide an intuitively appealing electronic argument in strong support of Barondeau and Lindahl's hypothesis[15] that the methyl group binds to the proximal rather than the distal Ni center of the A cluster. Additional computational evidence in support of methyl binding to Ni_p has recently been provided by Webster et al.,[11] although in their study, the electronic origin of this preference was not explored in detail. Notably, our computations reveal further that the Ni−C bond of the sterically and energetically most favorable Ni_p^{2+}−CH_3 adduct considered (model **4**) is similar in strength to the Co−C bond of the MeCbi^+ cofactor of CH_3−CoFeSP. Although an evaluation of the energetics of the methyl transfer from CH_3−CoFeSP to ACS (eq 2) would also require a consideration of the demethylated, reduced corrinoid and A cluster forms, the similar strengths of the Ni−C and Co−C bonds may constitute an important prerequisite for the reversibility of this transfer reaction. Thus, for the electronic reasons discussed above, the conformational flexibility of the A cluster that permits the proximal Ni center to adopt a square-planar conformation upon methylation may be crucial for the formation of a stable Ni−C bond, thereby allowing Ni_p to compete effectively with the Co^+ nucleophile for the methyl group used in ACS catalysis.

Acknowledgment. R.S. gratefully acknowledges a postdoctoral fellowship from the Swiss National Science Foundation. T.C.B. thanks the University of Wisconsin−Madison and the Sloan Research Foundation Fellowship Program for generous support. C.G.R. acknowledges generous financial support by the NIH.

Supporting Information Available: Atomic coordinates of models **1**−**5** (Tables S1−S8), key bond lengths and angles for **1** (Table S9), results from a NCA using different band assignments (Tables S10 and S11), contour plot of χ^2 from fits of the VTVH curves as a function of D and E/D (Figure S1), comparison of computed TD-DFT absorption spectra (Figure S2), depiction of the normal modes of **1** (Figure S3), total energies and spin densities for models **2**−**4** (Table S12), and key MOs of models **3a** and **4** (Figure S4). This material is available free of charge via the Internet at http://pubs.acs.org.

IC0483996

---

(65) Smith, A. K. In *Comprehensive Organometallic Chemistry II*; Abel, E. W., Stone, F. G. A., Wilkinson, G., Eds.; Elsevier Science Ltd.: Tarrytown, NY, 1995; Vol. 9, pp 1−28.

(66) (a) Tan, X. S.; Sewell, C.; Lindahl, P. A. *J. Am. Chem. Soc.* **2002**, *124*, 6277−6284. (b) Tan, X. S.; Sewell, C.; Yang, Q.; Lindahl, P. A. *J. Am. Chem. Soc.* **2003**, *125*, 318−319.